Crystal structure, lattice dynamics and thermodynamic properties of thermoelectric orthorhombic BaCu2Se2 compound

Romain Viennois, D. Bérardan, C. Popescu

Crystal structure, lattice dynamics and thermodynamic properties of thermoelectric orthorhombic $BaCu_2Se_2$ compound

R. Viennois[1,*] , D. Bérardan[2,*], C. Popescu[3]

[1] *ICGM, Univ Montpellier, CNRS, Ecole Nationale Supérieure de Chimie de Montpellier, Montpellier, France*

[2] *ICMMO (UMR 8182 CNRS), Université Paris-Sud, Université Paris-Saclay, F-91405 Orsay, France*

[3] *CELLS-ALBA Synchrotron Light Facility, Carrer de la Llum 2-26, 08290 Cerdanyola del Vallès, Barcelona, Spain*

Abstract

In the present work, we report a combined experimental and ab-initio study of the crystal structure, lattice dynamics and thermodynamic properties of the thermoelectric orthorhombic $BaCu_2Se_2$ compound. The thermal and pressure evolution of the crystal structure is obtained using synchrotron XRD experiments. The lattice dynamics is studied through Raman scattering experiments and ab-initio supercell calculations and reveals that the lowest Raman-active and infrared-active optical modes are at about 50 cm^{-1} (7 meV) and the presence of an optically silent low-energy optical mode at about 5 meV. From the determination of the heat capacity, the thermal expansion and the bulk modulus, a Grüneisen parameter of about 2.03 is estimated. This rather large value together with the presence of low energy optical modes and rather low Debye temperature in orthorhombic $BaCu_2Se_2$ can explain its low thermal conductivity. Additionally, we have also studied the lattice dynamics, the thermodynamic properties and the stability of the metastable tetragonal $BaCu_2Se_2$ against the stable orthorhombic phase and found that it might be stabilized at high temperature or high pressure.

Keywords: thermoelectric, chalcogenide, lattice dynamics

* Corresponding author: romain.viennois@umontpellier.fr

Corresponding author: david.berardan@icmmo.ups.fr

I. Introduction

Because of the problem of long-term energy supply and of global warming, there is a need to develop sustainable and green energy sources. Among them, thermoelectricity has attracted lots of interest particularly since one decade. This is due to the development of new performant thermoelectric materials with larger Figure of Merit Z. The efficiency of thermoelectric materials is characterized by their dimensionless Figure of Merit $ZT = \alpha^2 \sigma T / (\kappa_e + \kappa_l)$, with α the Seebeck coefficient, σ the electrical conductivity, κ_e and κ_l the thermal conductivity of the charge carriers and of the lattice, respectively. [1-3] Among the best thermoelectric materials, many are made of chalcogen atoms and more particularly of tellurium, such as the alloys based on Bi_2Te_3 in the temperature range close to room temperature or the PbTe based alloys and TAGS/LAST alloys in the 400-700 K temperature range. [1-4] At higher temperature, Si-Ge alloys are mainly used but chalcogenide based alloys such as La_3Ch_4 were found to have ZT slightly larger than 1 above 1100 K. [1,5,6] However, the use of tellurium is one obstacle against the large scale use of thermoelectric generators based on such telluride alloys because of its toxicity, scarcity and cost. [7,8] Hence, there has been a tremendous search of new chalcogenide alloys based on selenium or sulfur. La_3Ch_4-based alloys was one of the first families investigated for replacing Te by other chalcogen atoms,[1] and one of the authors showed using ab-initio calculations that La_3S_4 and La_3Se_4 should have similar thermoelectric properties as La_3Te_4. [6] For one decade, many new promising thermoelectric selenide alloys have been discovered. One of the first new compounds was In_4Se_{3-x} with ZT as large as 1.48 at 705 K. [4,9] However, the In-Se phase diagram indicates that In_4Se_3 is a line peritectic compound and the eutectic line between In_4Se_3 and In, a large mobility chemical specie, is as low as 429 K. [10] Therefore poor longtime stability is expected in these In_4Se_{3-x} samples. Thus, this stability issue in the temperature range with large ZT and the large cost of indium[7,8] question the possible application of In_4Se_{3-x} at large scale. Following the discovery of large ZT of 1.5 at about 1000 K in $Cu_{2-x}Se$[11], the superionic conductors based on Cu or other mobile ions have largely been explored. [12,13] However, if the large ionic mobility is helpful for strongly

reducing the thermal conductivity of these materials[11-13], this makes them also unstable under large dc currents and unsuitable for applications. [14,15] Very recently, SnSe has strongly attracted the attention because very large ZT was reported along the c axis, mainly because of a very low thermal conductivity. [16-18] Another advantage of this material was the possibility to obtain n-type alloys with large values of ZT. [19] However, there has been a controversy about the actual value of the thermal conductivity in single-crystalline materials, which is still open [16-18,20-24], and the performance of polycrystalline materials, which would be used in the design of thermogenerator, is much lower but still similar to those of the best PbTe-based alloys in the case of p-type SnSe alloys. [25,26] Moreover, this material undergoes a phase transition at about 800 K [16], and the stability of this material was also questioned. [20] In recent years, several studies also reported promising ZT values in some mineral-based multinary copper sulfides. [27,28]

One of the authors has recently also highlighted two new classes of promising selenide alloys (BiOCuSe [29-31] and α-$BaCu_2Se_2$ [32]) based on Cu-Se bondings but with no ionic mobility of Cu ions. BiCuSeO exhibits a good thermal stability until at least 900 K. [33] However, this is not the case for $BaCu_2Se_2$ for which some volatilization begins above 473 K, [32] and would thus require protective coating. In both cases, promising ZT values are observed and are directly linked to intrinsically very low values of the thermal conductivity. In the first family of compound, ZT as large as 1.4 at 900 K was found for p-type $Bi_{1-x}Sr_xCuSeO$ alloys with oriented grains. [30,31] It was recently found the possibility to obtain n-type materials of this family by using iron as n-type dopant, making it even more attractive. [34] In the case of the second class of compounds, ZT as large as 1 at 773 K was found for p-type orthorhombic α-$Ba_{1-x}Na_xCu_2Se_2$. [32] An attempt to improve the thermoelectric properties of the orthorhombic α-$BaCu_2Se_2$ phase by doping with K instead of Na did not permit to get higher ZT but lower ZT of 0.315 at 800 K for 30 % of K substitution on Ba site. [35] These promising thermoelectric properties were found for alloys derived from the orthorhombic α-$BaCu_2Se_2$ phase, which is a semiconducting parent compound with an energy bandgap of about 1.3 eV. [36-39] There also exists a metastable tetragonal β-$BaCu_2Se_2$ phase with the same crystal structure of $ThCr_2Si_2$ type as the parent compounds AFe_2As_2 (A = alkaline-earth) of the 122 iron based superconducting phase [36,37,40,41]

and whose energy bandgap was predicted to be slightly larger than for the orthorhombic α-$BaCu_2Se_2$ phase. [37] The thermoelectric properties of sulfide and telluride $BaCu_2Ch_2$ compounds were also studied but the best ZT obtained for the K-doped tetragonal β-$BaCu_2S_2$ compounds (ZT = 0.28 at 800 K) [42] was much lower than for the best selenide compounds, whereas the Seebeck coefficient of the orthorhombic α-$BaCu_2Te_2$ compound was rather low, [38] meaning that the potential of this last compound for thermoelectric applications is weak. Some other semiconducting Ba-Cu-Ch compounds with complex crystal structure exist, [43-48] but few of them have been investigated for their thermoelectric properties. However, two groups have reported very low thermal conductivity (< 1 W/m.K) in some of these compounds. [47,48] Notably, Kleinke's group reported ZT values as large as 0.8 at 600 K for $BaCu_{5.9}SeTe_6$. [47] Despite promising thermoelectric properties found for the orthorhombic α-$BaCu_2Se_2$ [32] and promising predictions from ab-initio calculations for this class of materials, [36,37] these materials have been very few investigated yet.

Pressure offers exciting opportunities for achieving high performance thermoelectric materials proving to be an useful tool to tune their properties as its temperature counterpart. Thus, the application of high pressure can alter the transport properties of thermoelectrics enhancing their performance parameters. In particular, high pressure effects were reported for BiCuSeO by theoretical calculations predicting a pressure-driven enhancement of the power factor at 700K. [49] Experimentally, it was showed that HP-HT synthesis at 3 GPa significantly improves the figure of merit of undoped BiCuSeO reaching ZT ~0.4 at 800 K. [50]

In the present work, we investigate for the first time the stability of the orthorhombic α-$BaCu_2Se_2$ phase under pressure both experimentally and theoretically and compare it with the case of the tetragonal β-$BaCu_2Se_2$ phase which was studied theoretically. We also report for the first time the lattice dynamics of both compounds from *ab-initio* calculations and compare with Raman experiments performed for the orthorhombic α-$BaCu_2Se_2$ phase and with the atomic displacement parameters obtained by neutron diffraction. From the thermodynamic properties obtained by *ab-initio* calculations, we are able to explain the origin of the higher thermal stability of the orthorhombic α-$BaCu_2Se_2$ phase and to give insights into the origin of its low thermal conductivity.

II. Methods

The density functional (DFT) calculations were carried out using the Vienna *ab initio* Simulation Package (VASP). [51] The calculations use potentials constructed with the scalar relativistic all-electron Blöchl's projector-augmented waves (PAW) technique [52] within the Perdew-Berke-Erzenhof parameterization (PBE) of the generalized gradient approximation (GGA). [53] A plane-wave energy cut-off of 350 eV and the tetrahedron numerical method have been applied. [54] We have used very fine 11x21x11 and 15x15x5 **k**-point samplings generated using the Monkhorst-Pack method [55] for the relaxation structure calculations for the orthorhombic α-$BaCu_2Se_2$ and the tetragonal β-$BaCu_2Se_2$ phases, respectively. The structures were relaxed until the residual forces were less than 10^{-4} eV/Å and the total energies were converged numerically to less than 10^{-10} eV. In order to determine the equation of states of both compounds, series of calculations of the energy have been performed for different fixed volumes while keeping the shape of the cell and the atomic positions free to relax. Otherwise, the calculation conditions are the same as for the structure relaxation. In order to determine the Bulk modulus and its derivative, we have used the Vinet equation in order to fit the equation E = f(V). [56] The present work did not concentrate on the electronic properties of the two $BaCu_2Se_2$ phases as this has been well done previously using GGA, meta-GGA and hybrid exchange-correlation functionals. [36,37] However, we report now the energy bandgap obtained from our DFT calculations: 0.44 eV for the orthorhombic α-$BaCu_2Se_2$ and 0.39 eV for the tetragonal β-$BaCu_2Se_2$ phases. We find a slightly smaller value for the tetragonal β-$BaCu_2Se_2$ phase than for the orthorhombic α-$BaCu_2Se_2$ phase, in qualitative agreement with the ref. 37. As expected with DFT calculations, our values are significantly smaller than the experimental value found for the orthorhombic α-$BaCu_2Se_2$ phase [38] and than the computed values found using hybrid exchange-correlation functional. [37] The lattice dynamics calculations were performed using the direct method with the supercell approach as described by Parlinski et al. [57] The calculations were performed on a 1x2x1 supercell containing 40 atoms with a grid of 11x11x11 **k**-mesh for the orthorhombic phase and on a 2x2x1 supercell containing 40 atoms and built from the conventional cell with a grid of 9x9x5 **k**-mesh for the quadratic phase. Prior to the

Hellmann-Feynman force calculations, the atomic positions were relaxed until the residual forces were less than 10^{-4}eV/Å^2. The Hellmann-Feynman forces were calculated for atomic displacements of 0.03 Å. For the dynamical matrix diagonalization and the subsequent lattice dynamics and thermodynamic calculations, we have used the Phonon code of Parlinski. [57]

The $BaCu_2Se_2$ sample was obtained by a two-step solid-state synthesis starting from Na_2Se, BaSe, Cu and Se precursors. In the first step, the Na_2Se and BaSe precursors were prepared and in the second step all precursors were thoroughly milled and mixed and then heated at 958 K for 48 h in sealed carbon-coated silica tubes under argon. After these thermal treatments, the samples were densified by Spark Plasma Sintering with a holding time of 10min at 723K under 100 MPa. The obtained samples were characterized by X-ray diffraction (XRD) and scanning electron microscopy coupled to energy dispersive X-ray spectroscopy (SEM+EDX). The samples were almost single-phase, containing minor fractions of β-Cu_2Se (about 0.5 %) and of an un-identified phase that could only be detected in the synchrotron-XRD patterns (see Figure 1). More details of the synthesis and structural characterization of the samples can be found in ref. 32. Raman scattering experiments have been performed using two different Raman spectrometers. We have firstly used a Labram Aramis spectrometer with backscattering geometry and using three different 473 nm, 633 nm and 785 nm lasers in order to study the effect of the resonant effect on the intensity of the Raman modes. However, as it is difficult to study the lower energy Raman modes with that spectrometer, we have also used a T64000 spectrometer from Horiba-Jobin Yvon in backscattering geometry and triple-monochromator configuration and using the 488 nm laser. Using the triple-monochromator configuration enabled us to study all the low energy Raman modes of $BaCu_2Se_2$. The error in Raman frequencies is about 2 cm^{-1} in the case of measurements with blue lasers (473 and 488 nm) and about 1 cm^{-1} in the case of measurements with the infrared laser (785 nm).

We performed two kinds of XRD experiments: (i) at room pressure and low temperature and (ii) high pressure and room temperature. Synchrotron XRD experiments were performed at MSPD beamline of Alba Synchrotron using both powder diffraction and high pressure end-stations. [58] Data at

RP and LT were collected at powder diffraction end-station using high-resolution mode through the 13 channels multi-analyzer crystals detector. In order to minimize absorption, incident X-rays with a wavelength of 0.3754 Å was used. The sample was enclosed in a glass capillary of 0.5 mm while data were registered on cooling at several temperatures between 295 K and 10 K and on heating up to 400K. Low temperatures were achieved using a liquid nitrogen cryostream (Oxford Cryosystems Series 700) and a so-called Dynaflow He flow cryostat. [59] The RT−HP XRD measurements were performed at the second end-station dedicated for HP measurements in diamond-anvil cells (DACs). The diffraction data were collected using a wavelength of 0.4246 Å (Sn K-edge) compressing the sample up to 23 GPa using a diamond-anvil cell (DAC) with diamond culets of 400 µm diameter. The $BaCu_2Se_2$ sample was placed together with Cu grains inside of a 180 µm diameter hole in the stainless steel gasket, pre-indented to 35 µm thickness. The EOS of Cu was used as a pressure scale with an accuracy of 0.1 GPa. [60] Two-dimensional diffraction images were collected using a SX-165 Rayonix CCD located at 240 mm away from the sample. The detector geometry was calibrated using LaB6 standard using FIT 2D software [61] while the resulting 1D patterns were analyzed by LeBail fitting using Fullprof software. [62]

Specific heat measurements were performed using a Quantum Design Physical Properties Measurement System (PPMS) from 400K to 300K using apiezon H grease and from 300K to 2K using apiezon N grease.

III. Results and discussion

III.A. Crystal structure

The temperature dependence of the lattice parameters of orthorhombic α-$BaCu_2Se_2$ obtained from the Rietveld refinement of our synchrotron data are reported in Fig. 2 whereas the atomic volume and the ratios *b*/*a* and *c*/*a* are reported in the supplementary informations. The X-ray patterns are reported in the supplementary information together with a representative example of the Rietveld refinements. The thermal variation of the interatomic distances and interatomic angles are reported in

the supplementary information. Note that measurement errors are lower than the size of the symbols in the Fig. 2 and in the supplementary information. The thermal variation of the Atomic Displacements Parameters (ADPs) will be discussed later on. The values found for the lattice parameters at room temperature agree very well with prior works. [32,38,40,63] Between 10 and 400 K, the ratio *b/a* is only slightly increasing from 0.4386 to 0.4392, whereas the ratio *c/a* is slightly decreasing from 1.1239 to 1.1230. The agreement of our data with prior high temperature experiments [32] is rather good. However, the coefficients of thermal expansion extracted from the linear fitting of our data between 200 and 400 K are significantly smaller than those obtained in ref. 32 for room temperature. Thus between 200 and 400 K, one finds the following thermal expansion coefficients: α_a = 20.2 ± 0.2 MK^{-1}, α_b = 23.9 ± 0.3 MK^{-1}, α_c = 18.1 ± 0.2 MK^{-1} and α_V = 62.2 ± 0.7 MK^{-1}. However, our present results confirm the weak anisotropy of the thermal expansion of orthorhombic $BaCu_2Se_2$. As our present data are of better quality and extended on larger temperature range, we believe that they are more reliable. Indeed, one finds very good quality factor for the linear fitting in the 200-400 K range (higher than 0.999). From the lattice parameters extracted from the XRD data, one can also determine the thermal variation of the thermal expansion in Figure 3. Here also, the errors for the thermal expansion are lower than the size of the symbols in the Figure 3. The thermal expansion becomes constant above 200 K, which is related to the low Debye temperature of about 230-255 K (see below).

Comparing our experimental results at 10 K (300 K) with our results from DFT calculations and prior DFT calculations for orthorhombic $BaCu_2Se_2$ (see Table 1), one finds that the calculated lattice parameters are larger by about 1.1-1.3 % (0.6-0.9 %) compared to experimental values at 10 K (295 K), which is quite reasonable. The agreement with the experiments at 10 K is much better than for the case of prior DFT calculations which overestimate the lattice parameters by about 0.9 % (for *b*) to 1.9-2 % for the calculations with revPBE+U exchange-correlation functional and by about 2.4-2.6 % for the calculations with HSE06 exchange-correlation functional. [36,37] For the case of tetragonal β-$BaCu_2Se_2$, similarly, as can be seen in Table 1, our calculated lattice parameters are in much better agreement with the room temperature experimental lattice parameters [40] than the lattice parameters calculated by Zhou et al with both revPBE+U and HSE06 exchange-correlation functionals. [37]

X-ray diffraction experiments under high pressure performed using synchrotron radiation on orthorhombic α-$BaCu_2Se_2$ were carried up to 23 GPa. In the whole pressure range covered in the study the only remarkable changes in the XRD patterns are represented by the gradual shift of the Bragg reflections toward higher values of 2θ due to cell parameters contraction. The initial phase is thus retained and no evidences of structural transition were found across the pressure range investigated in the present study, i. e. up to 23 GPa. Above 13 GPa, the Bragg peaks broaden as a consequence of the loss of hydrostaticity and the appearance of the deviatoric stress; however, this is expected when using 16:3:1 methanol-ethanol-water as pressure transmitting medium. [64,65] Moreover, the refinements carried out for pressures above 13 GPa yielded lattice parameters with significant uncertainty and thus we will constrain our data analysis to the hydrostatic regime. The pressure dependence of the experimental atomic volume is reported in Fig. 4 together with the pressure dependence of the atomic volume obtained with DFT calculations. One can see that if the volume is slightly larger for the DFT calculations, both curves follow the same trend. This is also the case for the different lattice parameters and their ratio (see the SI). The error bars for the volume, lattice parameters and their ratio as well as the pressure are lower than the size of the symbols in the Fig. 4 as well as in the SI. Note that the experimental and calculated *b/a* ratios are the same until 5 GPa. In both cases, the *b/a* and *c/a* ratios increase with pressure and the experimental ratios *b/a* and *c/a* increases by about 3.4 % and 2.7 % at 12 GPa. From the modelling of the experimental data with the Vinet equation [56,66] (see Fig. 4), using a room pressure atomic volume V_0 = 21.74 $Å^3$, one obtains a bulk modulus B = 60.4 ± 3.5 GPa and its pressure derivative dB/dP = 5 ± 0.7. From the modelling of the energy vs volume curves obtained by DFT calculations with the Vinet equation, one obtains a bulk modulus B = 56 GPa and its pressure derivative dB/dP = 5 (see SI). From these parameters, one can calculate the volume vs pressure curves shown in Fig. 4, which reproduces very well the results from the DFT calculations. We have also calculated the bulk modulus B and its pressure derivative dB/dP for the tetragonal β-$BaCu_2Se_2$ by modelling the energy vs pressure curves obtained by DFT calculations with the Vinet equation. If the atomic volume at room pressure V_0 of the tetragonal phase is slightly larger than that of the orthorhombic phase (see also Table 1), surprisingly, one finds almost the same B (= 55 GPa)

and dB/dP (= 5.1) for the tetragonal phase than for the orthorhombic phase. Hence, we expect that if it occurs, the high-pressure phase transition from the orthorhombic phase to the tetragonal phase will take place at pressure larger than 20 GPa. We have used two different methods for determining the transition pressure. Firstly, as the equations of states calculated with the DFT have been modeled with the Vinet equations, we can obtained the pressure at which both curves are crossing and find 21.5 GPa (see Fig. S12). Another method is to calculate the Gibbs energies, G = E + PV +TS, for both phase with the DFT (i. e. at 0 K) and from the difference of the Gibbs energy of the two phases ΔG, we find 24.8 GPa (see Fig. S13). However, we do not find traces of such phase transition in our experimental data within the whole pressure range of our study. The proposed HP transition could be shifted to higher transition pressures than predicted because of the presence of kinetic barriers. [67]

III.B. Lattice dynamics

We report in Fig. 5 (a) the Raman spectra for two different wavelengths (785 and 473 nm) using the Labram spectrometer. The same zone of the sample was examined and one can see a significant resonant effect. Thus, different vibrational modes can be highlighted. With the infrared laser (785 nm), the two peaks at 85 and at about 120 cm^{-1} are enhanced. As our experimental set-up did not permit us to access to the lower energy Raman modes, we have performed additional experiments with a triple-monochromator spectrometer. Thus, additional peaks can be observed at lower energy, located at 58 and 72 cm^{-1}. A broad beak is observed around 220-240 cm^{-1}, although our calculations do not evidence any vibrational modes above 200 cm^{-1} (see below). Therefore, several different areas of the sample have been analyzed. This broad feature changes significantly from one analysis to another, and is even almost vanishing in some Raman spectra (not shown). Therefore, we assign it to the presence of the unidentified secondary phases. Thus, the Raman modes of orthorhombic $BaCu_2Se_2$ are located between 50 and 200 cm^{-1}.

We have performed lattice dynamics calculations for both the orthorhombic and tetragonal $BaCu_2Se_2$ compounds.

The space group of the orthorhombic phase is P n m a (n° 62) and it contains 20 atoms in its primitive cell giving 60 different vibrational modes. The irreducible representations of the vibrational modes can be decomposed as following:

$$\Gamma_{vib} = 10\ A_g \oplus 5\ B_{1g} \oplus 10\ B_{2g} \oplus 5\ B_{3g} \oplus 5\ A_u \oplus 10\ B_{1u} \oplus 5\ B_{2u} \oplus 10\ B_{3u}$$

Among these modes, there are three acoustical modes ($B_{1u} \oplus B_{2u} \oplus B_{3u}$), 22 infrared and hyper-Raman active modes ($9\ B_{1u} \oplus 4\ B_{2u} \oplus 9\ B_{3u}$), 30 Raman active modes ($10\ A_g \oplus 5\ B_{1g} \oplus 10\ B_{2g} \oplus 5\ B_{3g}$) and 5 only hyper-Raman active modes ($5\ A_u$). The energies of the different vibrational modes are reported in Table 2.

As there are many Raman modes for the orthorhombic phase, the mode assignment using Raman spectroscopy data on powdered sample is not straightforward despite the present calculations. Our calculations indicate that the energies of the first order phonon modes range from 50 to 190 cm^{-1}, showing that the broad peak observed above 200 cm^{-1} has a different origin, either second order vibrational mode or from secondary phases. The last scenario is more probable because of the large sample dependence of this broad feature, which almost disappeared in some of our measurements (not shown). As indicated before, in the synchrotron XRD pattern, there are some traces of cubic β-Cu_2Se as well as of an unidentified phase. The cubic β-Cu_2Se has only one sharp Raman mode at about 260 cm^{-1} and therefore one could exclude it. [68] Thus, the broad feature at about 230-250 cm^{-1} can come perhaps from the unidentified phase. There is another possibility, this could be the amorphous Se phase or possibly disordered hexagonal Se phase located in the grain boundaries because their most intense Raman modes at about 230-250 cm^{-1} (depending of wavelength and power) [69-70] is located in the same energy range as the broad peak in our Raman spectra. It was maybe produced during the SPS process and located in the grain boundaries.

The space group of the tetragonal phase is I 4/m m m (n° 139) and it contains 5 atoms in its primitive cell giving 15 different vibrational modes. The irreducible representations of the vibrational modes can be decomposed as following:

$$\Gamma_{vib} = A_{1g} \oplus B_{1g} \oplus 2\ E_g \oplus 3\ A_{2u} \oplus 3\ E_u$$

Among these modes, there are three acoustical modes ($A_{2u} \oplus E_u$), 4 infrared and hyper-Raman active modes ($2\ A_{2u} \oplus 2\ E_u$) and 4 Raman active modes ($A_{1g} \oplus B_{1g} \oplus 2\ E_g$). In the different vibrational modes of both materials, the motions of all different types of atoms are involved. The energies of the different vibrational modes are reported in Table 2.

Now, we compare the phonon dispersion curves and density of states of both phases (see Figs. 6 and 7). The width of the optical phonon branches is slightly larger in the orthorhombic phase (5 to 23 meV) than in the tetragonal phase (7 to 22 meV) whereas the acoustical branches extend up to about 7 meV for both materials. In the case of the orthorhombic phase (Figs. 6 and 7), the Ba atoms and the different types of Cu atoms dominate the Phonon DOS (PDOS) for the energies up to 12 meV. Between 10 and 12 meV, the contribution of the Ba atoms is dominant, whereas there is a dominant contribution from the Se1 atom for the peak at about 13 meV. Above 16 meV, the contribution from the Ba atoms become very small whereas the contributions from the different types of Se atoms become dominant with still some contribution from Cu atoms. When looking at the features at low energy, one sees a small peak at about 3.5 meV, which is due to the acoustical modes at the vicinity of the Z and U points. The two lower energy optical modes at about 5 meV have different symmetries than that of the acoustical modes. This means that these optical modes could not hybridize with the acoustical modes. The strong peak at about 7 meV in the PDOS of the orthorhombic phase is due to both the flattening of some of the acoustical branches around the Y point and in the TR direction in this energy range and to some optical modes. These features are very favorable for strong scattering of the acoustical phonons by optical phonons as in the case of other materials with similar dispersion curves such as e. g. ZnSb. [71,72] However, the lattice thermal conductivity is several times lower in orthorhombic $BaCu_2Se_2$ (0.8 W/m.K at RT and down to 0.4 W/m.K at 750 K) [32] than in ZnSb. [73] Because both materials have similar number of atoms in the unit cell and similar low symmetry, this should be due to other effects such as larger anharmonicity, larger disorder, … . In the tetragonal phase (Fig. 7), the contribution of the Ba atoms is very dominant for the sharp and strong low energy peak at about 5 meV. Contrary to the case of the orthorhombic phase, this low energy peak is only due to the flattening of the lowest energy transverse acoustical mode at the Brillouin zone boundaries

(mainly around the P, N and X points) within a very significant part of the phase space. This means that a very large fraction of this acoustical branch loses its phase and do not contribute to heat transport. It is very favorable for a reduced thermal conductivity in this tetragonal phase, despite its higher symmetry and lower number of atoms in the primitive as compared to the orthorhombic phase. Note that this is the Ba PDOS projected along c direction which mainly contribute to this peak and that the Ba PDOS is strongly anisotropic with the energy of the vibrations of Ba along the z direction, i. e. between the Cu-Se layers being much smaller than the vibrations of Ba parallel to the layers. This should be related to the layered nature of the tetragonal phase. The peak at about 7-8 meV is dominated by the contribution of the copper and selenium atoms and is due to both the flattening of the transverse and longitudinal acoustical mode close to the X and P points and also to the lowest energy optical mode. The large peak at about 9 meV is dominated by the copper atoms, whereas the rather flat PDOS between 11 and 13 meV is dominated by the Ba atoms. Above 14 meV, there is no contribution from the Ba atoms and the contribution of Se atoms is dominating above 16 meV.

III.C. Thermodynamic properties

In Fig. 8 (a), we report the experimental heat capacity of orthorhombic α-$BaCu_2Se_2$ from 400K down to 2 K together with the heat capacity calculated from DFT calculations using the harmonic approximation for both the orthorhombic and tetragonal phases. In the Fig. 8, the error bars are smaller than the used symbols. In Fig. 8 (b) we show the same data plotted as a Debye plot for highlighting the deviation from a simple Debye model for which the heat capacity follows a T^3 dependence. The agreement between calculations and experiments for orthorhombic α-$BaCu_2Se_2$ is reasonable although not great. Note that above 260 K, the experimental data are larger than the high-temperature Dulong-Petit limit. The deviation at high temperature can come from several contributions that are not taken into account by the harmonic calculations performed at constant volume. In our experiments, the heat capacity measurements are performed under constant pressure (C_P) and we must take into account the difference between C_P and C_V that come from the thermal

expansion effect. Other effects to be taken into account are the anharmonicity and the defects, as this was made by several works for the case of ZnSb. [71,72,74] In our case, as we have determined the experimental value of the volume thermal expansion α_V and of the bulk modulus B at room temperature, we can calculate the experimental heat capacity at constant volume C_V above 200 K from: $C_V = C_P - \alpha_V^2 BVT$. One can see in Fig. 8 (a) an excellent agreement between the experimental and computed C_V of the orthorhombic phase. At low temperature, in both experiment and calculations, one sees in the Debye plot a deviation from the constant value expected with the Debye model. In the experiment, one sees a maximum at about 15-20 K, a temperature range in agreement with the 16.5 K obtained from DFT. In the case of the tetragonal phase, the maximum is located at lower temperature (13.5 K). This was expected as in the PDOS of the tetragonal phase, there is a large peak at about 5 meV whereas it is at about 7 meV for the orthorhombic phase. As this last value is similar to the case of the Ba_8Si_{46} clathrate, it is not surprising to see that this phase has a peak in the Debye plot of the heat capacity at about 16 K, [75] a value very close to what we find for orthorhombic $BaCu_2Se_2$.

From both the experimental and calculated low-temperature heat capacity data, one can determine the Debye temperature θ_D^C with a linear fitting of C/T vs T^2. [76] For the orthorhombic phase, we obtain θ_D^C = 253.2 K and 231.65 K for the experimental and the DFT data, respectively. The calculated value is smaller by about 10 %, which is expected because of the larger values of the calculated lattice parameters. The order of magnitude is very similar to that of thermoelectric antimonides such as ZnSb, [71,72] $LaFe_4Sb_{12}$ [77] or thermoelectric chalcogenides such as La_3Ch_4 (Ch = S, Se, Te). [6] For the tetragonal phase, the calculated Debye temperature θ_D^C is smaller and equal to 191.3 K. Another way to determine the Debye temperature is to calculate the mean vibrational energy <E> from the phonon density of states g(E) using: [78]

$$\theta_D^{DOS} = \frac{4}{3}\langle E \rangle = \frac{4}{3}\frac{\int g(E)EdE}{\int g(E)dE}$$

By this way, from our calculated PDOS, one finds θ_D^{DOS} = 207.5 K and 187.4 K for the orthorhombic and tetragonal phases, respectively. This is in reasonable agreement with the calculations from the low-temperature heat capacity.

In Fig. 9 (a), we report the thermal variation of the isotropic Atomic Displacement Parameters (ADPs) obtained from our synchrotron XRD experiments and compared with our calculated results. There is an overall qualitative agreement between experiments and calculations and we find in both cases that the ADPs of the Cu atoms are the largest ones and the ADPs of the Se atoms are the smallest ones. If the experimental ADPs of the Ba compare well with the calculated ADPs, this is not the case concerning the ADPs of the Cu and Se atoms for which the experimental values are typically underestimated by 0.005 $Å^2$. When looking at the anisotropic ADPs, one finds sometimes different trends between the experimental and calculated data, as can be seen in the Table 3 where the room temperature data are compared. In this Table, we also show the room temperature ADPs obtained for both the orthorhombic and the tetragonal phases by Huster and Bronger with single-crystalline samples. [40] Their results for the orthorhombic phase compare very well with our calculated data and even the detailed anisotropy of the ADPs they found is well reproduced by our calculations. We note that they found slightly smaller ADPs than the calculated ADPs and this can be account by the stronger bonding in the experimental structure due to its smaller lattice parameters. However, for the tetragonal phase, there is strong disagreement between our calculated ADPs with their experimental ADPs, even at the qualitative level. We find still much larger ADPs for the copper atoms than for the barium atoms in the case of the tetragonal phase as it was found for the orthorhombic phase, whereas Huster and Bronger found that the ADPs of the barium atoms become the largest in the tetragonal phase. [40] We have no explanation for this disagreement. In all compounds, the ADPs of the selenium atoms are the smallest.

The ADPs of the copper atoms in the orthorhombic phase seem rather large (0.015-0.02 $Å^2$) and have the same magnitude than in BiCuChO (Ch = S, Se, Te) [79,80] and in Cu_3SbSe_4 [81] with much larger thermal conductivity (about 3 W/m.K). [82] As discussed by some of us in the case of BiCuChO, [80] this does not mean that Cu atoms are rattling atoms. However, the ADPs of Cu are even much larger in the copper chalcogenides with mobile Cu atoms, such as β-$Cu_{2-x}Se$, [83] Cu_3SbSe_3 [84] and $Cu_{12+x}Sb_4S_{13}$, [85-87] than in BiCuChO and $BaCu_2Se_2$.

The experimental ground state of $BaCu_2Se_2$ is the orthorhombic phase, the tetragonal phase being metastable. However, as reported about 20 years ago by Huster and Bronger, both phases can be obtained under single-crystalline form using a flux of potassium-selenocyanate at 480°C. [40] Our DFT calculations show that at 0 K without the vibrational contribution, the orthorhombic phase is more stable than the tetragonal phase by about 3.12 kJ/mole.K. This difference is reduced to 2.93 kJ/mole.K when taking into account the zero point vibrational energy. This energy difference is quite small and can explain why Huster and Bronger have been able to grow single-crystals of the tetragonal phase. This also suggests that it could be possible to obtain the tetragonal phase by some out-of-equilibrium techniques such as e. g. mechanical alloying. Indeed, one of the present authors has already reported the synthesis of some metastable phases with similar small energy difference compared to the stable phase using mechanical alloying. [88,89] We have calculated the enthalpy difference ΔH as a function of temperature taking into account the vibrational entropy in the harmonic approximation (see SI). Our calculations suggest a possible phase transition from the orthorhombic phase to the tetragonal phase at about 950 K. Our own experimental study indicate the stability of the orthorhombic phase and the absence of phase transition until at least 873 K. [32] To the best of our knowledge, there has been no study investigating the stability of orthorhombic β-$BaCu_2Se_2$ above this temperature to date. Note that the anharmonicity, which is not taken into account in the present calculations, becomes larger at high temperature and could modify the transition temperature between the orthorhombic and the tetragonal phase. Note also that for the case of $BaCu_2S_2$, there is a phase transition from the orthorhombic to the tetragonal phase at about 813±10 K. [40] Both for $BaCu_2S_2$ and $BaCu_2Se_2$, there is no relationship between the space group Pnma of the orthorhombic phase and I4/mmm of the tetragonal phase. This means that the phase transition between both crystal structures will not be displacive but must be reconstructive and of first order. As usually pressure and temperature play an opposite role in the structural evolution, our DFT results are somehow unusual. However, there is the example of elemental calcium. It has face centered cubic structure at room conditions and has body centered cubic structure above 730 K at room pressure and this structure becomes stable at room temperature and for pressure higher than 20 GPa. [90,91]

As the thermal expansion is related to the anharmonicity, we have compared in Table 4 the thermal expansion and the thermal conductivity at room temperature of orthorhombic β-$BaCu_2Se_2$ to those of other thermoelectrics and in particular other copper chalcogenides. [11,31,32,80,92-98] One can see that the thermal expansion of β-$BaCu_2Se_2$ is slightly larger than that of PbTe [98] and slightly smaller than that of BiCuSeO [80], $AgSbTe_2$ [95] and β-$Cu_{2-x}Se$ [93] with the three last compounds having slightly smaller lattice thermal conductivity whereas the thermal conductivity of PbTe is 3-4 times larger. [98] We also note that the thermal expansion is much larger than in Cu_3SbSe_4 [95], $Cu_{12}Sb_4S_{13}$ [85,93] and SnSe. [96]

In order to have a better insight of the anharmonicity, we have determined the Grüneisen parameter Γ. In the present work, we have only determined the isotropic Grüneisen parameter because we do not know all the elastic constants whose knowledge is mandatory for determining the anisotropic Grüneisen parameters. [99] From the knowledge of the volume thermal expansion α_V at constant temperature, of the heat capacity at constant pressure C_P, of the molar volume V and of the bulk modulus B at constant temperature (here room temperature), we can determine the isotropic thermodynamic Grüneisen parameter Γ using: [99] $\Gamma = \alpha_V V B / C_P$. One finds $\Gamma = 2.03 \pm 0.14$ at room temperature, which is a rather large value. The thermal variation of Γ is given in SI. Similar values of the Grüneisen parameter and thermal conductivity have been found in the case of $AgSbTe_2$ [97] whereas the Grüneisen parameter is slightly larger and the thermal conductivity is slightly smaller in the case of BiCuSeO. [31,80] Significantly smaller Grüneisen parameter is found in the case of β-$Cu_{2-x}Se$ [93] despite its slightly smaller thermal conductivity. [11]

In order to discuss qualitatively the origin of the low thermal conductivity of orthorhombic $BaCu_2Se_2$, we can use the Slack formula in order to obtain an estimation, despite its limitations, which have been discussed elsewhere. [72,80] The Slack formula is written as following: [78] $\kappa_l = A M_{at} (V_{at})^{1/3} \theta_D^3 / T (n^{1/3}\Gamma)^2$, where M_{at} is the average atomic mass, V_{at} is the volume per atom, θ_D is the Debye temperature, A is a constant equal to 3.04×10^{-8} s^{-3} K^{-3}, n is the number of atoms in the primitive cell, and Γ is the Grüneisen parameter. In the above formula, the thermal conductivity is obtained in

W/cmK if the volume is given in $Å^3$ and the average atomic mass in amu. Using the experimental value of the Debye temperature and of the isotropic thermodynamic Grüneisen parameter obtained at room temperature, we find κ_l = 1.93 W/m.K at 300 K. This value is about 2 times larger than the experimental value of the thermal conductivity. [32] Such overestimation of the thermal conductivity using the Slack formula is well-known. [72,78] Despite this problem, the Slack formula give semi-quantitative results that enable to find the good trend between different compounds. [72,78]

IV. Conclusion

In the present work, we report a combined experimental and ab-initio study of the crystal structure, lattice dynamics and thermodynamic properties of thermoelectric orthorhombic structure $BaCu_2Se_2$. The thermal and pressure evolution of the crystal structure is reported using synchrotron XRD experiments. Our results show that the initial orthorhombic α-$BaCu_2Se_2$ remains stable within the whole pressure range of this study. Experimental and calculated bulk moduli are in good agreement. The lattice dynamics is studied through Raman scattering experiments and ab-initio supercell calculations and reveals that the lowest Raman-active and infrared-active optical modes are at about 50 cm^{-1} (7 meV) and the presence of an optically silent low-energy optical mode at about 5 meV. From the determination of the heat capacity, the thermal expansion and the bulk modulus, one finds that a Grüneisen parameter of about 2.03 at room temperature. This rather large value together with the presence of low energy optical modes and rather low sound velocities in orthorhombic $BaCu_2Se_2$ can explain its low thermal conductivity. Last, we have also studied the lattice dynamics, the thermodynamic properties and the stability of the metastable tetragonal $BaCu_2Se_2$ against the stable orthorhombic phase and found that it is a high temperature phase and would become the most stable phase above 950 K, similarly to the case of the $BaCu_2S_2$ compounds. However, this temperature may be underestimated as we did not take into account to neither the volume effect nor the anharmonic effect.

V. Associated content

V. A. Supplementary informations

Synchrotron powder X-ray pattern of orthorhombic $BaCu_2Se_2$ in function of temperature. Example of Rietveld refinement of the synchrotron powder X-ray diffraction data of orthorhombic $BaCu_2Se_2$ at room temperature. Thermal variation of the atomic volume V_{at} and the ratios *b*/*a* and *c*/*a* of the orthorhombic α-$BaCu_2Se_2$ phase. Pictures of the crystal structure of orthorhombic $BaCu_2Se_2$ from the experimental data. Thermal variations of the different interatomic distances and interatomic angles of orthorhombic $BaCu_2Se_2$ from the analysis of the XRD data. Synchrotron powder X-ray pattern of orthorhombic $BaCu_2Se_2$ in function of pressure. Pressure variation of the lattice parameters and their ratio of orthorhombic $BaCu_2Se_2$. Variation of the atomic energy with the atomic volume for the two orthorhombic and tetragonal BaCu2Se2 phases obtained by DFT calculations. Pressure variation of the difference of Gibbs energy between the orthorhombic and tetragonal phases obtained by DFT calculations. Thermal variation of the difference of enthalpy between the orthorhombic and tetragonal phases obtained by DFT calculations. Thermal variation of the Grüneisen parameter.

Acknowledgement

The authors acknowledge the Alba synchrotron facility for providing beamtime on MSPD beamline. CP is thankful for the financial support of the Spanish Mineco Project FIS2017-83295-P.

References

[1] Woods, C., Materials for themoelectric energy conversion. *Rep. Progr. Phys*. **1988**, *51*, 459-539.

[2] Soostman, J. R.; Chung, D. Y.; Kanatzidis, M. G., New and Old Concepts in Thermoelectric Materials. *Angew. Chem. Int. Ed.* **2009**, *48*, 8616-8639.

[3] Tan, G.; Zhao, L.-D.; Kanatzidis, M. G., Rationally Designing High-Performance Bulk Thermoelectric Materials. *Chem. Rev.* **2016**, *116*, 12123-12149.

[4] Han, C.; Sun, Q.; Li, Z.; Dou, S. X., Thermoelectric Enhancement of Different Kinds of Metal Chalcogenides. *Adv. Energy Mater.* **2016**, *6*, 1600498.

[5] Ma, J. M.; Clarke, S. M.; Zeier, W. G.; Vo, T.; Von Allmen, P.; Snyder, G. J.; Kaner, R. B.; Fleurial, J. P.; Bux, S. K., Mechanochemical synthesis and high temperature thermoelectric properties of calcium-doped lanthanum telluride $La_{3-x}Ca_xTe_4$. *J. Mater. Chem. C* **2015**, *3*, 10459-10466.

[6] Viennois, R.; Niedziolka, K.; Jund, P., Physical properties of the thermoelectric cubic lanthanum chalcogenides $La_{3-y}X_4$ (X = S, Se, Te) from first principles. *Phys. Rev. B* **2013**, *88*, 174302.

[7] Amatya, R.; Ram, R. J., Trend for Thermoelectric Materials and Their Earth Abundance. *J. Electron. Mater.* **2012**, *41*, 1011-1019.

[8] Gaultois, M. W.; Sparks, T. D.; H. Borg, C. K.; Seshadri, R.; Bonificio, W. D.; Clarke, D. R., Data-Driven Review of Thermoelectric Materials: Performance and Ressource Considerations. *Chem. Mater.* **2013**, *25*, 2911-2920.

[9] Rhyee, J.-S.; Lee, K. H.; Lee, S. M.; Cho, E.; Kim, S. I.; Lee, E.; Kwon, Y. S.; Shim, J. H.; Kotliar, G., Peierls distortion as a route to high thermoelectric performance in $In_4Se_{3-\delta}$ crystals. *Nature* **2009**, *459*, 965-968.

[10] Okamoto, H., In-Se (Indium-Selenium). *J. Phase Equil. Diff.* **2004**, *25*, 201.

[11] Liu, H.; Shi, X.; Xu, F.; Zhang, L.; Zhang, W.; Chen, L.; Li, Q.; Uher, C.; Day, T.; Snyder, G. J., Copper ion liquid-like thermoelectrics. *Nat. Mater.* **2012**, *11*, 422-425.

[12] Bayley, T. P.; Uher, C., Potentials for superionic conductors in thermoelectric applications. *Current Opinion in Green Sust. Chem.* **2017**, *4*, 58-63.

[13] Qiu, P.; Shi, X.; Chen, L., Cu-based thermoelectric materials. *Energy Mater. Stor.* **2017**, *3*, 85-97.

[14] Brown, D. R.; Day, T.; Caillat, T.; Snyder, G. J., Chemical Stability of $(Ag,Cu)_2Se$: a Historical Overview. *J. Electron. Mater.* **2013**, *42*, 2014-2019.

[15] Dennler, G.; Chmielowski, R.; Jacob, S.; Capet, F.; Roussel, P.; Zastrow, S.; Nielsch, K.; Opahle, I.; Madsen, G. K. H., Are Binary Copper Sulfides/Selenides Really New and Promising Thermoelectric Materials ?. *Adv. Energy Mater.* **2014**, *4*, 1301581.

[16] Zhao, L.-D.; Lo, S.-H.; Zhang, Y.; Sun, H.; Tan, G.; Uher, C.; Wolverton, G.; Dravid, V. P.; Kanatzidis, M. G, Ultralow thermal conductivity and high thermoelectric figure of merit in SnSe crystals. *Nature* **2014**, *508*, 373-377 ; see also the comment : Wei, P-C.; Bhattacharya, S.; He, J.; Neeleshwar, S.; Podila, R.; Chen, Y. Y.; Rao, A. M., The intrinsic thermal conductivity of SnSe. *Nature* **2016**, *539*, E1 and the reply : Zhao, L.-D.; Lo, S.-H.; Zhang, Y.; Sun, H.; Tan, G.; Uher, C.; Wolverton, G.; Dravid, V. P.; Kanatzidis, M. G., Zhao et al. Reply. *Nature* **2016**, *539*, E2.

[17] Zhao, L.-D.; Chang, C.; Tan, G.; Kanatzidis, M. G., SnSe: a remarkable new thermoelectric material. *Energy Environ. Sci.* **2016**, *9*, 3044-3060.

[18] Zhao, L.-D.; Tan, G.; Hao, S.; He, J.; Pei, Y.; Chi, H.; Wang, H.; Gong, S.; Xu, H.; Dravid, V. P.; Uher, C.; Snyder, G. J.; Wolverton, G.; Kanatzidis, M. G., Ultrahigh power factor and thermoelectric performance in hole-doped single-crystal SnSe. *Science* **2016**, *351*, 141-144.

[19] Duong, A. T.; Nguyen, V. Q.; Duvjir, G.; Duong, V. T.; Kwon, S.; Song, J. Y.; Lee, J. K.; Lee, J. E.; Park, S. D.; Min, T.; Lee, J.; Kim, J.; Cho, S., Achieving ZT = 2.2 with Bi-doped n-type SnSe single crystals. *Nat. Commun.* **2016**, *7*, 13713.

[20] Sassi, S.; Candolfi, C.; Vaney, J.-B.; Ohorodniichuk, V.; Masschelein, P.; Dauscher, A.; Lenoir, B., Assessment of the thermoelectric performance of polycrystalline of p-type SnSe. *Appl. Phys. Lett.* **2014**, *104*, 212105.

[21] Carrete, J.; Mingo, N.; Curtarolo, S., Low thermal conductivity and triaxial phononic anisotropy of SnSe. *Appl. Phys. Lett.* **2014**, *105*, 101907.

[22] Ibrahim, D.; Vaney, J.-B.; Sassi, S.; Candolfi, C.; Ohorodniichuk, V.; Levinsky, P.; Semprimoschnig, C.; Dauscher, A.; Lenoir, B., Reinvestigation of the thermal properties of single-crystalline SnSe. *Appl. Phys. Lett.* **2017**, *110*, 032103.

[23] Jin, M.; Shao, H.; Hu, H.; Li, D.; Shen, H.; Xu, J., Growth and characterization of of large size undoped p-type SnSe single-crystal by Horizontal Brigdman technique. *J. Alloys Compds* **2017**, *712*, 857-862.

[24] Wu, D.; Wu, L.; He, D.; Zhao, L.-D.; Li, W.; Wu, M.; Jin, M.; Xu, J.; Jiang, J.; Huang, L.; Zhu, Y.; Kanatzidis, M. G.; He, J., Direct observation of vast off-stoichiometric defects in single-crystalline SnSe. *Nano Energy* **2017**, *35*, 321-330.

[25] Wei, T.-R.; Tan, G.; Zhang, X.; Wu, C.-F.; Li, J.-F.; Dravid, V. P.; Snyder, G. J.; Kanatzidis, M. G., Distinct Impact of Alkali-Ion Doping on Electrical Transport Properties of Thermoelectric p-Type Polycrystalline SnSe. *J. Am. Chem. Soc*. **2016**, *138*, 8875-8882.

[26] Tang, G.; Wei, W.; Zhang, J.; Li, Y.; Wang, X.; Xu, G.; Chang, C.; Wang, Z.; Du, Y.; Zhao, L.-D., Realizing High Figure of Merit in Phase-Separated Polycrystalline $Sn_{1-x}Pb_xSe$. *J. Am. Chem. Soc.* **2016**, *138*, 13647-13654.

[27] Lu, X.; Morelli, D. T.; Xia, Y.; Zhu, F.; Ozolins, V.; Chi, H.; Zhou, X.; Uher, C., High Performance Thermoelectricity in Earth-Abundant Compounds Based on Natural Mineral Tetrahedrites. *Adv. Energy Mater.* **2013**, *3*, 342-348.

[28] Bourgès, C.; Bouyrie, Y.; Supka, A. R.; Al Rahal Al Orabi, R.; Lemoine, P.; Lebedev, O. I.; Ohta, M.; Suekuni, K.; Nassif, V.; Hardy, V.; Daou, R.; Miyazaki, Y.; Fornari, M.; Guilmeau, E., High-Performance Thermoelectric Bulk Colusite by Process Controlled Structural Disordering. *J. Amer. Chem. Soc.* **2018**, *140*, 2186-2195.

[29] Zhao, L. D.; Berardan, D; Pei, Y. L.; Byl, C.; Pinsard-Gaudart, L.; Dragoe, N., $Bi_{1-x}Sr_xCuSeO$ oxyselenides as promising thermoelectric materials. *Appl. Phys. Lett.* **2010**, *97*, 092118.

[30] Sui, J.; Li, J.; He, J.; Pei, Y.-L.; Berardan, D.; Wu, H.; Dragoe, N.; Cai, W.; Zhao, L.-D., Texturation boosts the thermoelectric performance of BiCuSeO oxyselenides. *Energy Environ. Sci.* **2013**, *7*, 2916-2920.

[31] Zhao, L.-D.; He, J.; Berardan, D.; Lin, Y.; Lin, J.-F.; Nan, C.-W.; Dragoe, N., BiCuSeO oxyselenides: new promising thermoelectric materials. *Energy Environ. Sci.* **2014**, *7*, 2900-2924.

[32] Li, J.; Zhao, L.-D.; Sui, J.; Berardan, D.; Cai, W.; Dragoe, N., $BaCu_2Se_2$ based compounds as promising thermoelectric materials. *Dalton Trans.* **2015**, *44*, 2285-2293.

[33] Barreteau, C.; Berardan, D.; Dragoe, N., Studies on the thermal stability of BiCuSeO. *J. Solid State Chem.* **2015**, *222*, 53-59.

[34] Pan, L.; Lang, Y.; Zhao, L.; Berardan, D.; Amzallag, E.; Xu, C.; Gu, Y.; Chen, C.; Zhao, L.-D.; Shen, X.; Lyu, Y.; Lu, C.; Wang, Y., Realization of n-type and enhanced thermoelectric performance of p-type BiCuSeO by controlled iron incorporation. *J. Mater. Chem. A* **2018**, *6*, 13340-13349.

[35] Zhang, H.; Li, S.; Li, D.; Ji, S.; Shen, S.; Ying, T.; Lin, Z.; Li, K.; Yuan, D.; Zhao, H., Enhancement of the thermoelectric properties of $BaCu_2Se_2$ by potassium doping. *Mater. Lett.* **2015**, *152*, 117-120.

[36] Krishnapriyan, A.; Barton, P. T.; Miao, M.; Seshadri, R., First-principles study of band alignments in the p-type hosts BaM_2X_2 (M = Cu, Ag ; X = Se, S). *J. Phys.: Condens. Matter.* **2014**, *26*, 155802.

[37] Zou, D.; Zheng, H.; Li, J., Comparative studies of the electronic structure and thermoelectric properties in orthorhombic and tetragonal $BaCu_2Se_2$ by first-principles calculations. *RSC Adv.* **2016**, *6*, 60717-60722.

[38] McGuire, M. A.; May, A. F.; Singh, D. J.; Du, M.-H.; Jellison, G. E., Transport and optical properties of heavily hole-doped semiconductors $BaCu_2Se_2$ and $BaCu_2Te_2$. *J. Solid State Chem.* **2011**, *184*, 2744-2750.

[39] Li, W.; Liu, Z.; Yang, G., First-principles study of electronic structure, elastic and anisotropic thermoelectric properties of $BaCu_2Se_2$. *J. Alloys Compds.* **2017**, *695*, 3682-3688.

[40] Huster, J.; Bronger, W., α- und β-$BaCu_2X_2$ (W = Se, S). Darstellung von Einkristallen in Kalliumchalkigenocyanat-Schmelzen. *Z. Anorg. Allg. Chem.* **1999**, *625*, 2033-2040.

[41] Rotter, M.; Tegel, M.; Johrendt, D.; Schellenberg, I.; Hermes, W.; Pöttgen, R., Spin-density-wave anomaly at 140 K in the ternary iron arsenide $BaFe_2As_2$. *Phys. Rev. B* **2008**, *78*, 020503.

[42] Kurosaki, K.; Uneda, H.; Muta, H.; Yamanaka, S., Thermoelectric properties of potassium-doped β-$BaCu_2S_2$ with natural superlattice structure. *J. Appl. Phys.* **2005**, *97*, 053705.

[43] Eliezer, Z.; Steinfink, H.,The electrical behavior of α and β $BaCu_4S_3$. *Mat. Res. Bull.* **1976**, *11*, 385-388.

[44] Ohtani, T.; Oshino, T.; Tsujinouchi, A.; Hasegawa, M.; Nagaoka, N.; Yokota, Y.; Okada, Y., Phase transition in the layered ternary copper sulfide [α $BaCu_4S_3$]. *Mat. Res. Bull.* **1995**, *30*, 161-167.

[45] Ouammou, A.; Mouallem-Bahout, M.; Pena, O.; Halet, J.-F.; Saillard, J.-Y.; Carel, C., Physical properties and Electronic Structure of Ternary Barium Copper Sulfides. *J. Solid State Chem.* **1995**, *117*, 73.

[46] Han, Y., Siol, S.; Zhang, Q.; Zakutaev, A., Optoelectronic Properties of Strontium and Barium Copper Sulfides Prepared by Combinatorial Sputtering. *Chem. Mater.* **2015**, *29*, 8239-8248.

[47] Oudah, M.; Kleinke, K. T.; Kleinke, H., Thermoelectric Properties of the Quaternary Chacogenides $BaCu_{5.9}STe_6$ and $BaCu_{5.9}SeTe_6$. *Inorg. Chem* **2015**, *54*, 845-849.

[48] Maier, S.; Perez, O.; Pelloquin, D.; Berthebaud, D.; Hebert, S.; Gascoin, F.,Linear, Hypervalent Se_3^{4-} Units and Unprecedented Cu_4Se_9 Building Blocks in the Copper(I) Selenide $Ba_4Cu_8Se_{13}$. *Inorg. Chem.* **2017**, *56*, 9209-9218.

[49] Zou, D.; Liu, Y.; Xie, S.; Lin, J.; Zheng, H.; Li, J., High pressure effect on the electronic structure and thermoelectric properties of BiCuSeO: first-principles calculations. *RSC Adv.* **2014**, *4*, 54819-54825.

[50] Zhu, H.; Li, Y.; Li, H.; Su, T.; Pu, C.; Zhao, Y.; Ma, Y.; Zhu, P.; Wang, X., Effects of high pressure sintering on the microstructure and thermoelectric properties of BiCuSeO. *High. Press. Res.* **2016**, *37*, 36-45.

[51] Kresse, G.; Furthmüller, J., Efficient iterative schemes for *ab initio* total-energy calculations using a plane-wave basis set. *Phys. Rev. B* **1996**, *54*, 11169-11185.

[52] Kresse, G.; Joubert, D., From ultrasoft pseudopotentials to the projector augmented-wave method. *Phys. Rev. B* **1999**, *59*, 1758-1775.

[53] Perdew, J. P.; Burke, K.; Erzenhof, M., Generalized Gradient Approximation Made Simple. *Phys. Rev. Lett.* **1996**, *77*, 3865-3868.

[54] Blöch, P. E.; Jepsen, O.; Andersen, O. K., Improved tetrahedron method for Brillouin-zone integration. *Phys. Rev. B* **1994**, *49*, 16223-16233.

[55] Monkhorst, H. J.; Pack, J. D., Special Points for Brillouin-Zone Integrations. *Phys. Rev. B* **1976**, *13*, 5188-5192.

[56] Vinet, P.; Rose, J. H.; Ferrante, J.; Smith, J. R., Universal features of the equation of states of solids. *J. Phys.: Condens. Matter* **1989**, *1*, 1941.

[57] Parlinski, K.; Li, Z.-Q.; Kawazoe, Y., First-Principles Determination of the Soft Mode in cubic ZrO_2. *Phys. Rev. Lett.* **1997**, *78*, 4063-4066.

[58] Fauth, F.; Peral, I.; Popescu, C.; Knapp, M. The new material science powder diffraction beamline at ALBA synchrotron. *Powder Diffr.* **2013**, *28*, S360−S370.

[59] van der Linden, P. J. E. M.; Moretti Sala, M.; Henriquet, C.; Rossi, M.; Ohgushi, K.; Fauth, F.; Simonelli, L.; Marini, C.; Fraga, E.; Murray, C.; Potter, J.; Krisch, M., A compact and versatile dynamic flow cryostat for photon science. *Rev. Sci. Instrum.* **2016**, *87*, 115103.

[60] Dewaele, A.; P. Loubeyre P.; Mezouar, M., Equations of state of six metals above 94 GPa, *Phys. Rev. B* **2004**, *70*, 094112.

[61] Hammersley, A. P., FIT2D: a multi-purpose data reduction, analysis, and visualization program. *J. Appl. Cryst.* **2016**, *49*, 646-652.

[62] Rodriguez-Carvajal, J., Magnetic Structure Determination from Powder Diffraction Using the Program Fullprof. *Applied Crystallography* **2001**, 30-36.

[63] Iglesias, J. E.; Pachali, K. E.; Steinfink, H., Structural Chemistry of Ba_2CdS_3, Ba_2CdSe_3, $BaCdS_2$, $BaCu_2S_2$, $BaCu_2Se_2$. *J. Solid State Chem.* **1974**, *9*, 6-14.

[64] Errandonea, D. ; Muñoz, A. ; Gonzalez-Platas, J., Comment on “High-pressure x-ray diffraction study of YBO_3/Eu^{3+}, $GdBO_3$, and $EuBO_3$: Pressure-induced amorphization in GdBO3” [J. Appl. 115, 043507 (2014)]. *J. Appl. Phys.* **2014**, *115*, 216101.

[65] Klotz, S.; Chervin, J. C.; Munsch, P.; Le Marchand, G., Hydrostatic limits of 11 pressure transmitting media. *J. Phys. D: Appl. Phys.* **2009**, *42*, 075413.

[66] Gonzalez-Plata, J. ; Alvaro, M. ; Nestola, F. ; Angel, R., EoSFit7-GUI: a new graphical user interface for equation of state calculations, analyses and teaching. *J. Appl. Cryst.* **2016**, *49*, 1377-1382.

[67] Bandiello, E. ; Errandonea, D. ; Pellicer-Pores, J. ; Garg, A. . ; Rodriguez-Hernandez, P. ; Muñoz, A. ; Martinez-Garcia, D. ; Rao, R. ; Popescu, C., Effect of High-Pressure on the Crystal Structure and Vibrational Properties of Olivine-Type $LiNiPO_4$. *Inorg. Chem.* **2018**, *57*, 10265-10276.

[68] Sajid Babu, N.; Abdul Khadar, M., Deposition of nanocrystal thin films of Cu_2Se and their optical and electrical characterization. *Appl. Surf. Sci.* **2019**, *474*, 34-41.

[69] Nagata, K.; Ishibashi, K.; Miyamato, Y., Raman and Infrared Spectra of Rhombohedral Selenium. *Jpn. J. Appl. Phys*. **1981**, *20*, 463-469.

[70] Carroll, P. J.; Lannin, J. S., Raman scattering of amorphous selenium films. *Solid State Commun.* **1981**, *40*, 81-84.

[71] Jund, P.; Viennois, R.; Tao, X. M.; Niedziolka, K.; Tedenac, J.-C., Physical properties of thermoelectric zinc antimonide using first-principles calculations. *Phys. Rev. B*, **2012** *85*, 224105.

[72] Hermet, P.; Koza, M. M.; Ritter, C.; Reibel, C.; Viennois, R., Origin of the highly anisotropic thermal expansion of the semiconducting ZnSb and relations with its thermoelectric applications. *RSC Adv*. **2015**, *5*, 87118.

[73] Fedorov, M. I.; Prokof'eva, L. V.; Pshenay-Severin, D. A.; Shabaldin, A. A.; Konstantinov, P. P., New Interest in Intermetallic Compound. ZnSb *J. Electron. Mater*. **2014**, *43*, 2314-2319.

[74] Fischer, A.; Scheidt, E.-W.; Scherer, W.; Benson, D. E.; Wu, Y.; Eklöf, D.; Häussermann, U., Thermal and vibrational properties of thermoelectric ZnSb: Exploring the origin of low thermal conductivity. *Phys. Rev. B* **2015**, *91*, 224309.

[75] Lortz, R.; Viennois, R.; Petrovic, A.; Wang, Y.; Toulemonde, P.; Meingast, C.; Koza, M. M.; Mutka, H.; Bossak, A.; San Miguel, A., Phonon density of states, anharmonicity, electron-phonon coupling, and possible multigap superconductivity in the clathrate superconductors Ba_8Si_{46} and $Ba_{24}Si_{100}$: Factors behind large difference in T_c. *Phys. Rev. B* **2008**, *77*, 224507.

[76] Ashcroft, N. W.; Mermin, N., *Solid State Physics.*; Saunders College Publishing, Harcourt College Publishers, Harcourt Inc., 1976.

[77] Viennois, R.; Charar, S.; Ravot, D.; Haen, P.; Mauger, A.; Bentien, A.; Paschen, S.; Steglich, F., Spin fluctuations in the skutterudite compound $LaFe_4Sb_{12}$. *Eur. Phys. J. B* **2005**, *46*, 257-267.

[78] Slack, G. A., The Thermal Conductivity of Nonmetallic Crystals. *Solid State Phys*. **1979**, *34*, 1-71.

[79] Vaqueiro, P.; Al Orabi, R. A. R.; Luu, S. D. N.; Guélou, G.; Powell, A. V.; Smith, R. I.; Song, J.-P.; Wee, D.; Fornari, M., The role of copper in the thermal conductivity of thermoelectric oxychalcogenides: do lone pairs matter?. *Phys. Chem. Chem. Phys.* **2015**, *17*, 31735-31740.

[80] Viennois, R.; Hermet, P.; Beaudhuin, M.; Bantignies, J.-L.; Maurin, D.; Pailhès, S.; Fernandez-Diaz, M. T.; Koza, M. M.; Barreteau, C.; Dragoe, N.; Bérardan, D., Lattice Dynamics Study of Thermoelectric Oxychalcogenide BiCuChO (Ch = Se, S). *J. Phys. Chem. C* **2019**, *123*, 16046-16057.

[81] Pfitzner, A., Crystal structure of tricopper tetraselenoantimonate (V), Cu_3SbSe_4. *Z. Krist.* **1994**, *209*, 685.

[82] Skoug, E. J.; Cain, J. D.; Morelli, D. T., Structural effects on the lattice thermal conductivity of ternary antimony- and bismuth-containing chalcogenide semiconductors. *Appl. Phys. Lett.* **2010**, *96*, 181905.

[83] Eikeland, E.; Blichfeld, A. B.; Borup, K. A.; Zhao, K.; Overgaard, J.; Shi, X.; Chen, L.; Iversen, B. B., Crystal structure across the β to α phase transition in thermoelectric $Cu_{2-x}Se$. *IUCrJ* **2017**, *4*, 476-485.

[84] Pfitzner, A., Cu_3SbSe_4: Synthese und Kristallstruktur. *Z. Anorg. Allg. Chem.* **1995**, *621*, 685-688.

[85] Pfitzner, A.; Evain, M.; Petricek, V., $Cu_{12}Sb_4S_{13}$: A Temperature-Dependent Structure Investigation *Acta Cryst. B* **1997**, *53*, 337-345.

[86] Lai, W.; Wang, Y.; Morelli, D. T.; Lu, X., From Bond Asymmetry to Anharmonic Rattling in $Cu_{12}Sb_4S_{13}$ Tetrahedrites: When Lone-Pair Electrons Are not So Lonely. *Adv. Funct. Mater.* **2015**, *25*, 3648-3657.

[87] Vaqueiro, P.; Guélou, G.; Kaltzoglou, A.; Smith, R. I.; Barbier, T.; Guilmeau, E.; Powell, A. V., The Influence of Mobile Copper Ions on the Glass-Like Thermal Conductivity of Copper-Rich Tetrahedrites. *Chem. Mater.* **2017**, *29*, 4080-4090.

[88] Esmilaire, R.; Beaudhuin, M.; Hermet, P.; Fréty, N.; Ravot, D.; Viennois, R., Synthesis and characterization of the semiconducting metastable phase Al_6Ge_5. *Mater. Lett.* **2015**, *138*, 222-224.

[89] Moll, A.; Beaudhuin, M.; Legrand, V.; Debord, R.; Pailhès, S.; Viennois, R.; Fréty, N., Mechanical alloying as a new synthesis route for metastable silicon clathrates. *Mater. Lett.* **2017**, *187*, 1-3.

[90] Errandonea, D. ; Boehler, R. ; Ross, M., Melting of the alkaline-earth metals to 80 GPa. *Phys. Rev. B* **2001**, *65*, 012108.

[91] Anzellini, S. ; Errandonea, D. ; McLeod, S. G. ; Botella, P. ; Daisenberger, D. ; De'Ath, J. M. ; Gonzalez-Platas, J. ; Ibañez, J. ; McMahon, M. I. ; Munro, K. A. ; Popescu, C.; Ruiz-Fuerte, J. ; Wilson, C. M., Phase diagram of calcium at high pressure and high temperature. *Phys. Rev. Mater.* **2018**, *2*, 083608.

[92] Kim, H.; Ballikaya, S.; Chi, H.; Ahn, J.-P.; Ahn, K.; Uher, C.; Kaviany, M., Ultralow thermal conductivity of β-Cu_2Se by atomic fluidity and structure distortion. *Acta Mater*. **2015**, *86*, 247-253.

[93] May, A. F.; Delaire, O.; Niedziela, J. L.; Lara-Curzio, E.; Susner, M. A.; Abernathy, D. L.; Kirkham, M.; McGuire, M. A., Structural phase transition and phonon instability in $Cu_{12}Sb_4S_{13}$. *Phys. Rev. B* **2016**, *93*, 064104.

[94] Heo, J.; Laurita, G.; Muir, S.; Subramanian, M. A.; Keszler, D. A., Enhanced Thermoelectric Performance of Synthetic Tetrahedrites. *Chem. Mater*. **2013**, *26*, 2047-2051.

[95] Madelung, O., *Semiconductors: Data Handbook*; Springer-Verlag Berlin Heidelberg GmbH, 2004.

[96] Popuri, S.R.; Pollet, M.; Decourt, R.; Viciu, L. M.; Bos, J. W. G., Evidence for hard and soft substructures in thermoelectric SnSe. *Appl. Phys. Lett*. **2017**, *110*, 253903.

[97] Morelli, D. T.; Jovovic, J.; Heremans, J. P., Intrinsically Minimal Thermal Conductivity in Cubic I-IV-VI_2 Semiconductors. *Phys. Rev. Lett.* **2008**, *101*, 035901.

[98] Houston, B.; Skrana, R. E.; Belson, H. S., Elastic Constants, Thermal Expansion, and Debye Temperature of Lead Telluride. *J. Appl. Phys*. **1968**, *39*, 3913-3916.

[99] Barron, T. H. K. ; Collins, J. G. ; White, G. K., Thermal expansion of solids at low temperatures, *Adv. Phys*. **1981**, *29*, 609-730.

Tables

Table 1 Lattice parameters of orthorhombic α-$BaCu_2Se_2$ obtained from our synchrotron XRD experiments at 10 and 295 K compared to prior experiments at room temperature[38,40,63] and to our own DFT calculations and prior DFT calculations[37] and of tetragonal β-$BaCu_2Se_2$ obtained from our DFT calculations and compared to prior experiments at room temperature[40] and prior DFT calculations. [37]

Compound	a (Å)	b (Å)	c (Å)	V_{at} (Å^3/at.)	E_{at} (eV/at.)	Comments
α-$BaCu_2Se_2$	9.66163	4.24144	10.88444	22.302	-4.1624	PBE (present work)
	9.557(1)	4.1915(5)	10.741(1)	21.51		10 K XRD
	9.600(1)	4.2140(5)	10.783(1)	21.81		295 K XRD
	9.5944(6)	4.2142(4)	10.7748(8)	21.783		single-crystal XRD [63]
	9.595(1)	4.208(1)	10.773(1)	21.745		single-crystal XRD [40]
	9.59999(8)	4.21381(3)	10.78361(9)	21.811		XRD [38]
	9.7485	4.2312	10.9469	22.577		RevPBE+U [37]
	9.8092	4.2952	11.011	23.196		HSE06 [37]
β-$BaCu_2Se_2$	4.0865	4.0865	13.21775	22.073	-4.1301	PBE (present work)
	4.040(1)	4.04	13.1855(33)	21.52		XRD monocr. [40]
	4.138	4.138	13.38	22.91		RevPBE+U [37]
	4.1394	4.1394	13.3942	22.95		HSE06 [37]

Table 2 Energies of the different types of vibrational modes (in cm^{-1}) for both orthorhombic α-$BaCu_2Se_2$ and tetragonal β-$BaCu_2Se_2$.

Compound	Raman-active modes	Infrared-active modes	Other modes	Comments
α-$BaCu_2Se_2$	58 ; 72 ; 84 ; 92 ; 101 ; 118-121 ; 130-145 ; 162 ; 187			Experiments
	A_g: 47.5 ; 54.4 ; 66.4 ; 79.5 ; 92.7 ; 112 ; 139.6 ; 153 ; 168.9 ; 179.4	B_{1u}: 56.6 ; 61.7 ; 86.5 ; 95.9 ; 108 ; 123.1 ; 142.3 ; 153.5 ; 171.3	A_u: 43.5 ; 59.6 ; 83.5 ; 105.9 ; 172.3	DFT
	B_{1g}: 53.7 ; 57.7 ; 74.7 ; 133.2 ; 180.3			
	B_{2g}: 68.7 ; 75 ; 82.6 ; 94.9 ; 100.6 ; 108.1 ; 128.7 ; 149.2 ; 176.9 ; 186.1	B_{2u}: 58.5 ; 87.6 ; 106.7 ; 172.7		
	B_{3g}: 50.9 ; 62.4 ; 80 ; 132.8 ; 180.3	B_{3u}: 62 ; 69.3 ; 85.6 ; 94 ; 117.9 ; 124.8 ; 138.6 ; 146.3 ; 171.5 ;		
β-$BaCu_2Se_2$	E_g: 47.6 ; 148.6	E_u: 66.7 ; 104.3		DFT
	B_{1g}: 94 ; A_{1g}: 170.7	A_{2u}: 78 ; 128.1		

Table 3 Atomic displacement parameters U_{ij} (in $Å^2$) of Ba, Cu and Se for both orthorhombic α-$BaCu_2Se_2$ and tetragonal β-$BaCu_2Se_2$. The experimental data of the present work are taken at 300 K.

Compound	Atom	U_{11} ($Å^2$)	U_{22} ($Å^2$)	U_{33} ($Å^2$)	U_{13} ($Å^2$)	U_{iso} ($Å^2$)	Comments
α-$BaCu_2Se_2$	Ba	0.0120(4)	0.0094(4)	0.0071(3)		0.0095(3)	Exp. (present work)
		0.0160(3)	0.0106(2)	0.0103(2)	-0.0007(2)	0.0123(3)	Exp. [40]
		0.0148	0.0099	0.0102	0.0006	0.0116	DFT
	Cu1	0.0176(8)	0.0141(9)	0.0114(7)		0.0144(8)	Exp. (present work)
		0.0208(6)	0.0139(6)	0.0165(5)	0.0040(4)	0.0171(6)	Exp. [40]
		0.0232	0.0154	0.0212	0.0056	0.0199	DFT
	Cu2	0.0122(7)	0.0209(8)	0.0127(7)		0.0153(8)	Exp. (present work)
		0.0164(5)	0.0199(6)	0.0136(5)	0.0012(4)	0.0166(6)	Exp. [40]
		0.0192	0.0238	0.0176	-0.0017	0.0202	DFT
	Se1	0.0096(6)	0.0062(5)	0.0018(5)		0.0059(5)	Exp. (present work)
		0.0119(4)	0.0094(4)	0.0074(4)	0.0000(3)	0.0096(4)	Exp. [40]
		0.0126	0.0103	0.0098	0.0005	0.0109	DFT
	Se2	0.00599(5)	0.0088(6)	0.0027(5)		0.0058(5)	Exp. (present work)
		0.0105(3)	0.0087(4)	0.0076(3)	-0.0005(3)	0.0089(4)	Exp. [40]
		0.0117	0.0096	0.0091	0.0003	0.0101	DFT
β-$BaCu_2Se_2$	Ba	0.026(1)	0.026(1)	0.031(2)		0.028(2)	Exp. [40]
		0.0131	0.0131	0.0284		0.0182	DFT
	Cu	0.015(1)	0.015(1)	0.016(2)		0.0153(20)	Exp. [40]
		0.0293	0.0293	0.0243		0.0276	DFT
	Se	0.0085(9)	0.0085(9)	0.008(1)		0.0083(10)	Exp. [40]
		0.0143	0.0143	0.0151		0.0146	DFT

Table 4 Volume thermal expansion, Grüneisen parameter and lattice thermal conductivity of α-$BaCu_2Se_2$ compared to several other chalcogenide compounds at room temperature. [11,31,32,78,80,85,92-95,97,98]

* In this case, the data are taken at 500 K.

Compound	α_V(300K) in MK^{-1}	Γ(300K)	κ_L(300K) in W/m.K
α-$BaCu_2Se_2$	62.2	2.03	0.7 [32]
BiCuSeO	67.4 [80]	2.27 [80]	0.55 [31]
β-$Cu_{2-x}Se$	75* [92]	1* [92]	0.6* [11]
$Cu_{12}Sb_4S_{13}$	40-43 [85,93]		0.25 [94]
Cu_3SbSe_4	37.2 [95]		1.46 [95]
$AgSbTe_2$	69 [95]	2.05 [97]	0.63[97]
PbTe	61.2 [98]	1.45 [78]	2.4 [97]

Figure captions

Figure 1: Rietveld refinement of the synchrotron powder X-ray pattern of orthorhombic $BaCu_2Se_2$ at 295 K. The peaks indicated by the blue circles in the magnified view correspond to secondary phases (open symbols = β-Cu_2Se, filled symbols = unidentified phase).

Figure 2 Thermal variation of the lattice parameters *a*, *b* and *c* of the orthorhombic α-$BaCu_2Se_2$ phase obtained from Rietveld refinement of synchrotron powder X-ray diffraction patterns.

Figure 3 Thermal variation of the thermal expansion α_x, α_y and α_z. Inset: thermal variation of the volume thermal expansion α_V.

Figure 4 Pressure variation of the atomic volume the orthorhombic α-$BaCu_2Se_2$ phase obtained from Rietveld refinement of synchrotron powder X-ray diffraction patterns and from DFT calculations (solid symbols) and fitted with the Vinet equations of states (lines).

Figure 5 Raman spectra using Labram spectrometer with infrared laser of λ = 785 nm (red curve) and blue laser of λ = 473 nm (blue curve) (a) and T64000 spectrometer with blue laser of λ = 488 nm (b) of the orthorhombic α-$BaCu_2Se_2$ phase compared with the positions of the calculated Raman-active modes (solid symbols).

Figure 6 Calculated phonon dispersion curves, total and atom-projected phonon Density of States of the orthorhombic α-$BaCu_2Se_2$ phase.

Figure 7 Calculated phonon dispersion curves, total and atom-projected phononDensity of States of the tetragonal β-$BaCu_2Se_2$ phase.

Figure 8 (a) Thermal variation of the experimental heat capacity of the orthorhombic phase and of the calculated heat capacity of the orthorhombic and tetragonal phase. (b) Debye plot of the experimental heat capacity of the orthorhombic phase and of the calculated heat capacity of the orthorhombic and tetragonal phase.

Figure 9 (a) Thermal variation of the experimental and calculated Atomic Displacement parameters of the orthorhombic phase. (b) Thermal variation of the calculated Atomic Displacement parameters of the tetragonal phase.

Figures

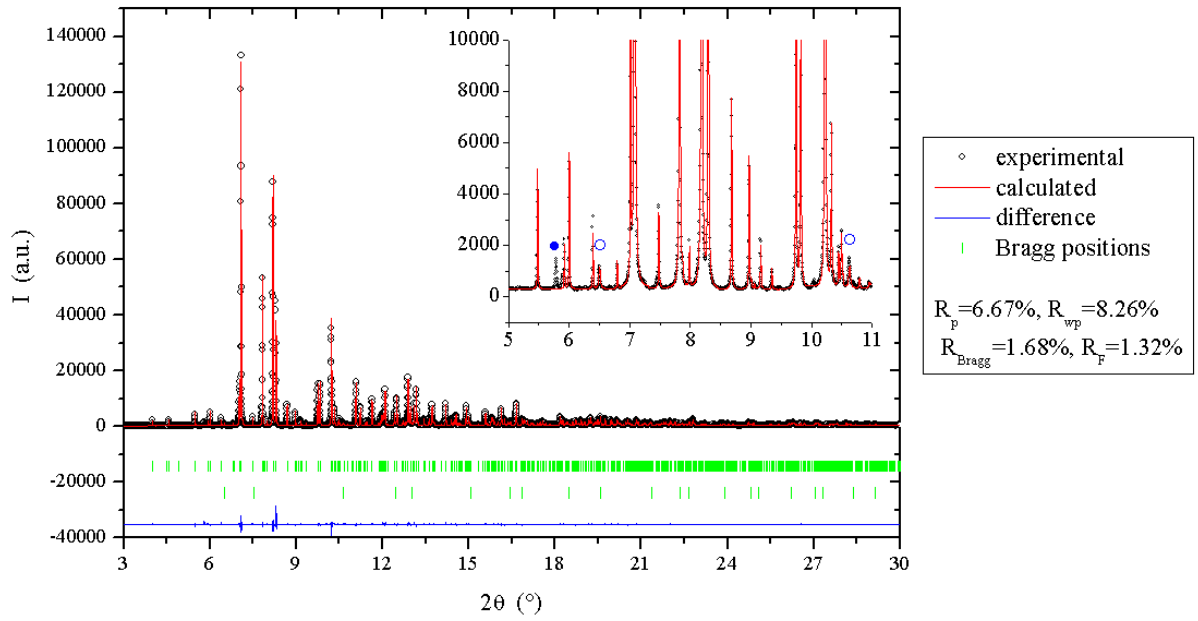

Figure 1

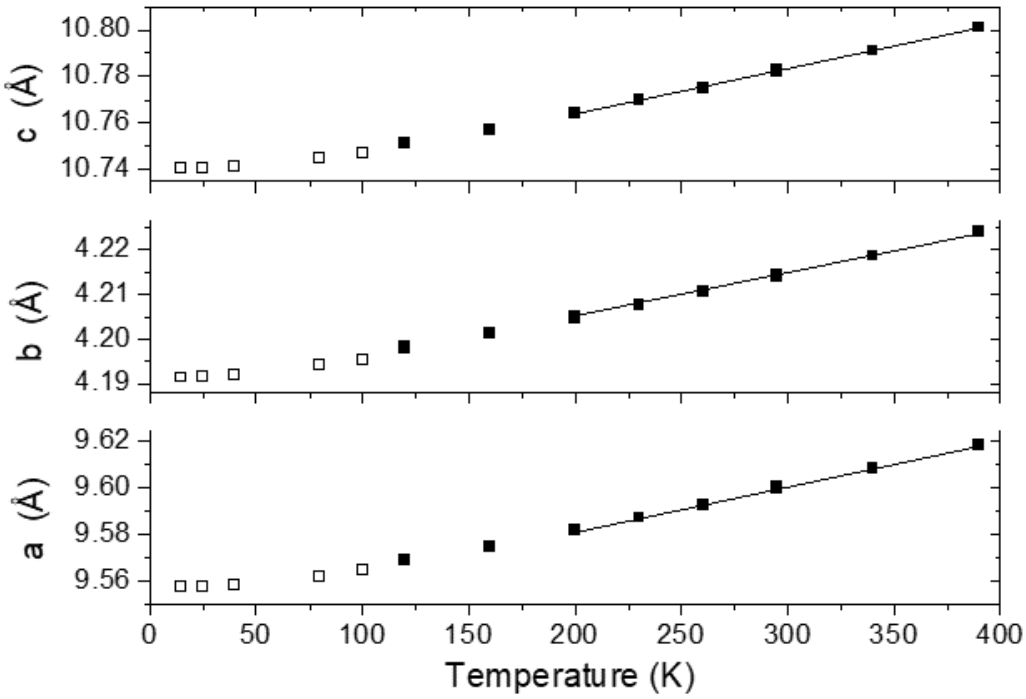
c (Å)
10.80
10.78
10.76
10.74
b (Å)
4.22
4.21
4.20
4.19
a (Å)
9.62
9.60
9.58
9.56
0
50
100
150
200
250
300
350
400
Temperature (K)

Figure 2

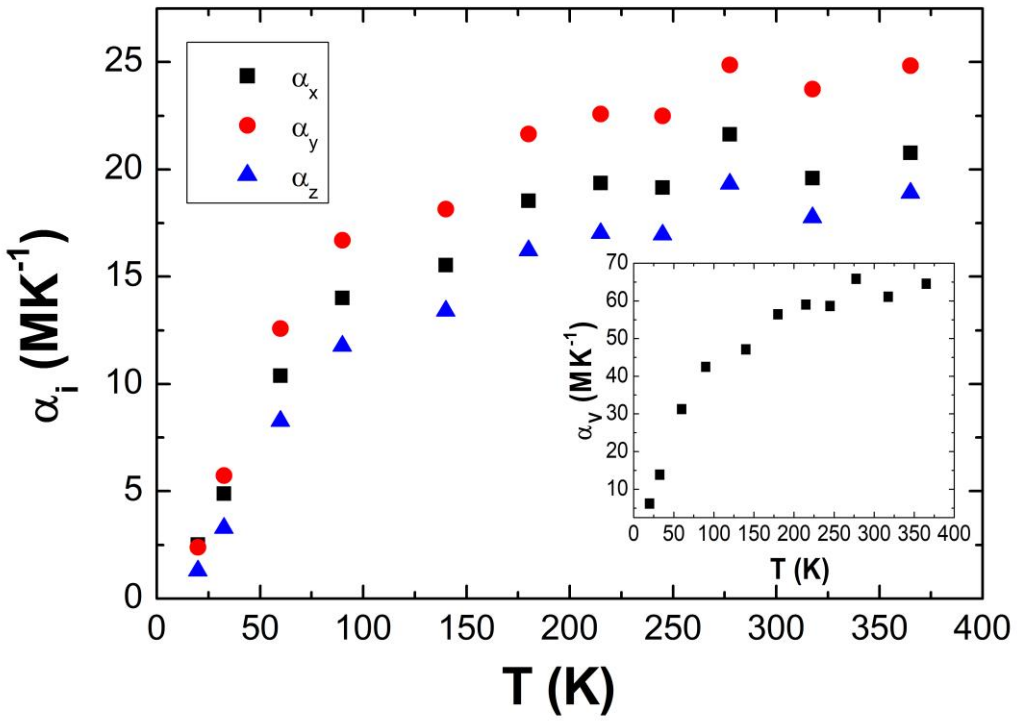

Figure 3

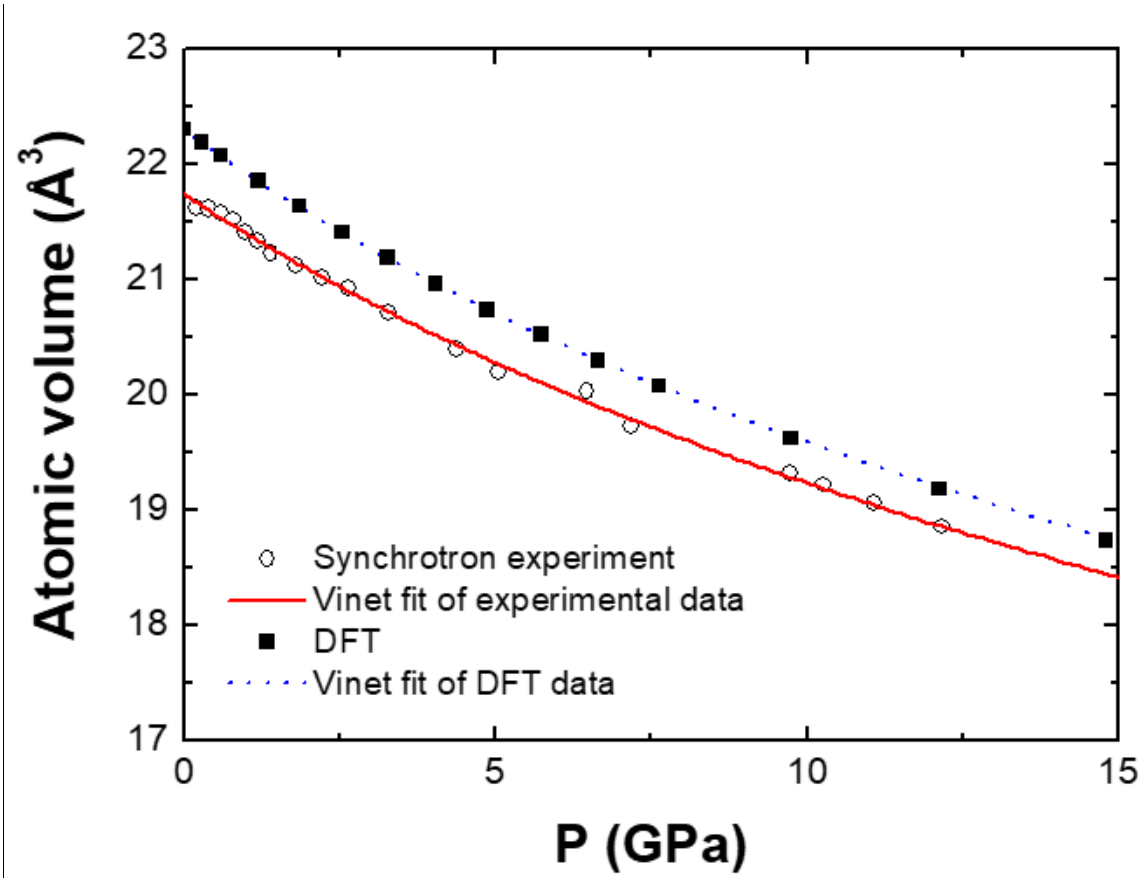
Atomic volume (A^3)
P (GPa)
Synchrotron experiment
Vinet fit of experimental data
DFT
Vinet fit of DFT data
23
22
21
20
19
18
17
0
5
10
15

Figure 4

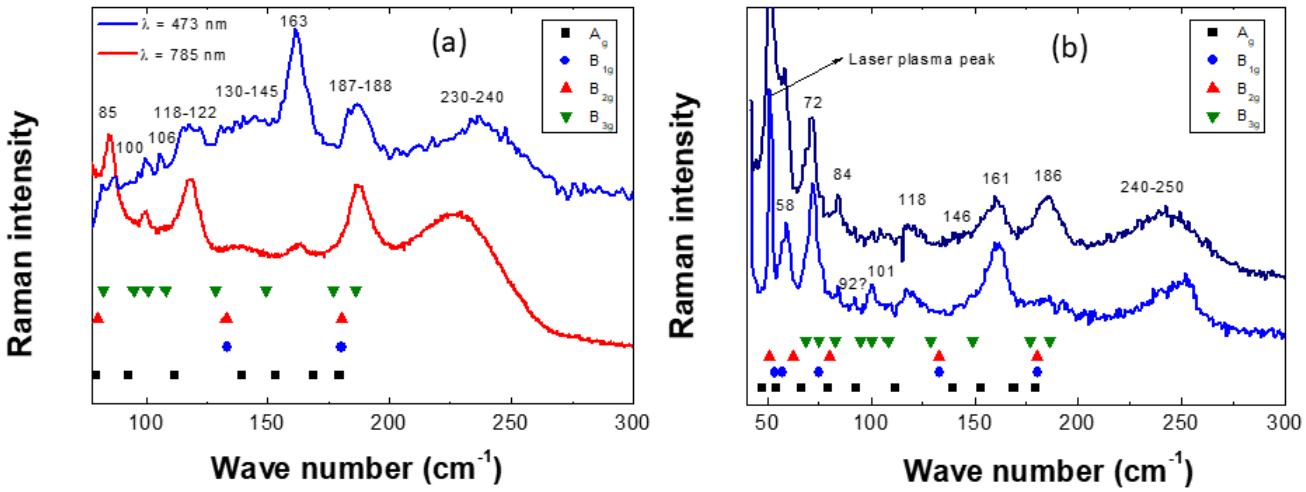
λ = 473 nm
λ = 785 nm
(a)
A g
B 1g
B 2g
B 3g
85
100
106
118-122
130-145
163
187-188
230-240
Raman intensity
Wave number (cm-1)
Laser plasma peak
(b)
72
58
84
92?
101
118
146
161
186
240-250

Figure 5

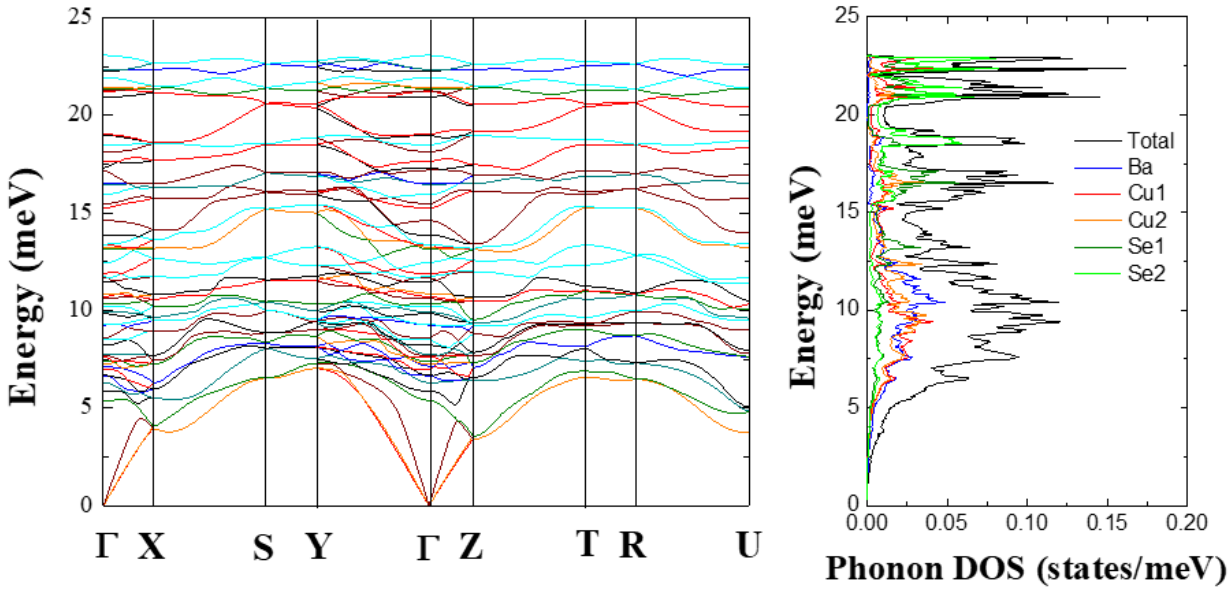
Energy (meV)
25
20
15
10
5
0
Γ X S Y Γ Z T R U
Energy (meV)
Total
Ba
Cu1
Cu2
Se1
Se2
0.00 0.05 0.10 0.15 0.20
Phonon DOS (states/meV)

Figure 6

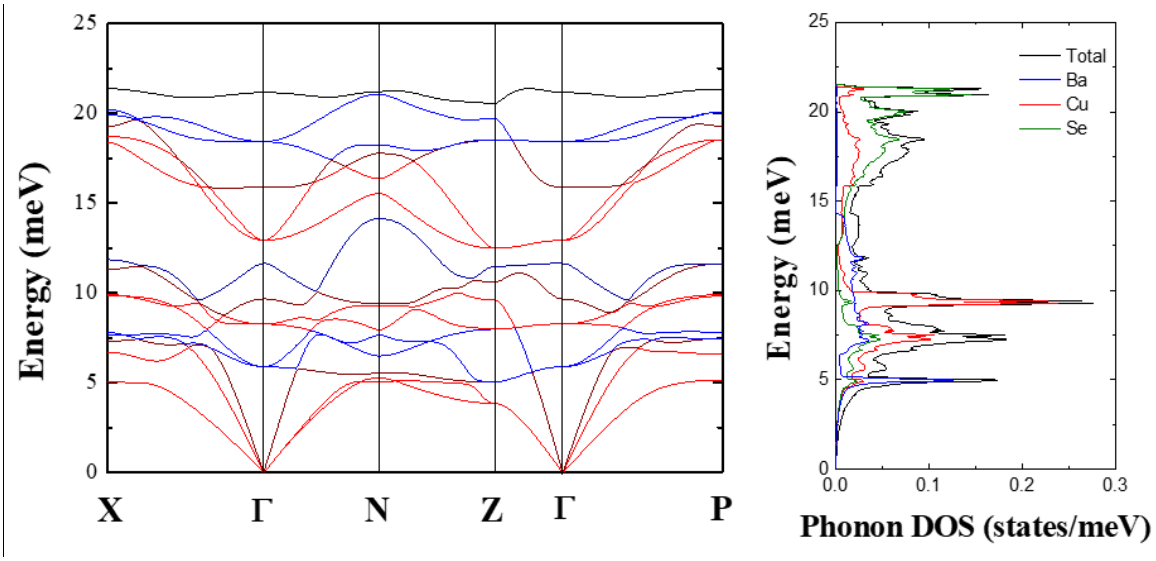
Energy (meV)
25
20
15
10
5
0
X
Γ
N
Z
Γ
P
Energy (meV)
Total
Ba
Cu
Se
0.0
0.1
0.2
0.3
Phonon DOS (states/meV)

Figure 7

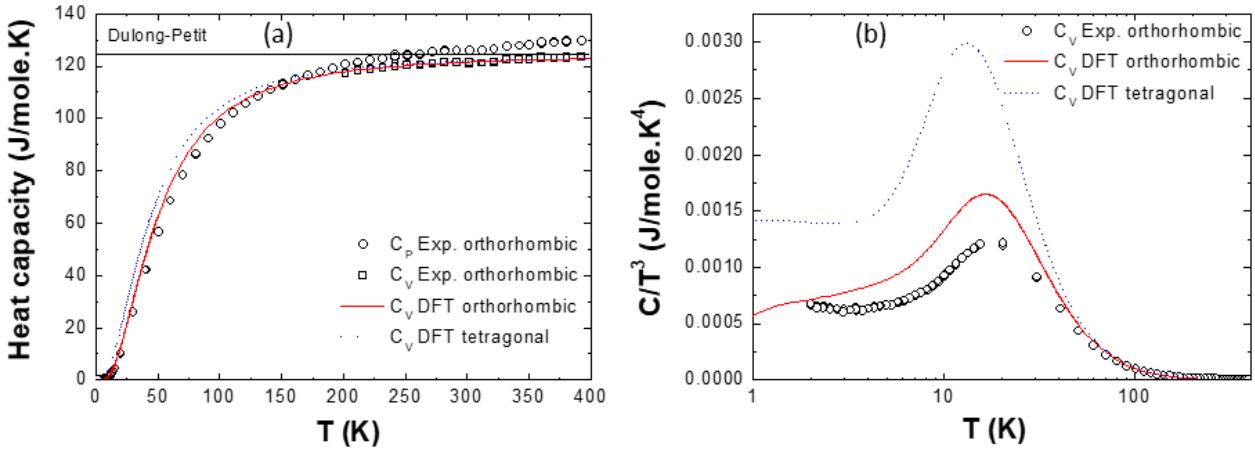
Heat capacity (J/mole.K)
Dulong-Petit
(a)
C_P Exp. orthorhombic
C_V Exp. orthorhombic
C_V DFT orthorhombic
C_V DFT tetragonal
T (K)
C/T^3 (J/mole.K^4)
(b)
C_V Exp. orthorhombic
C_V DFT orthorhombic
C_V DFT tetragonal
T (K)

Figure 8

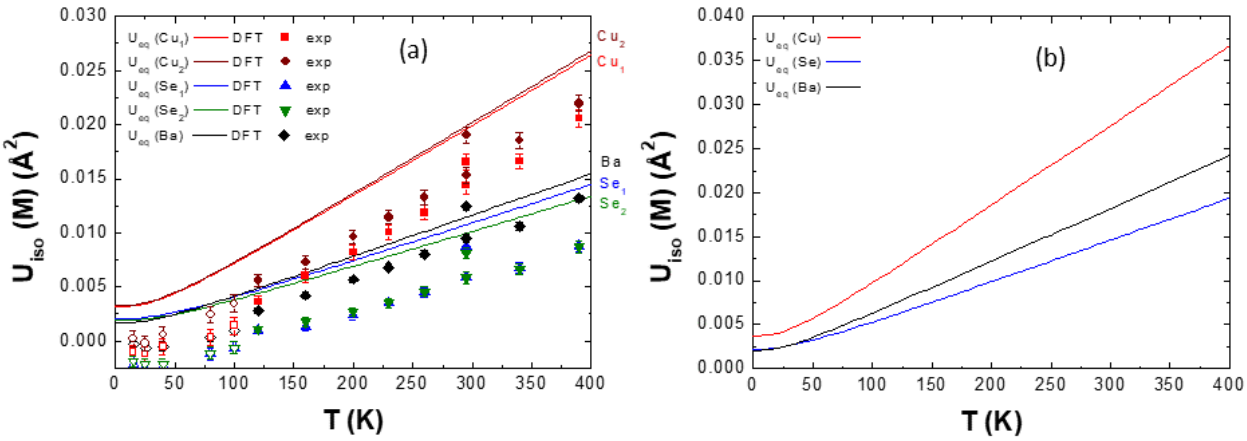
(a)
(b)
U_{eq} (Cu_1) DFT exp
U_{eq} (Cu_2) DFT exp
U_{eq} (Se_1) DFT exp
U_{eq} (Se_2) DFT exp
U_{eq} (Ba) DFT exp
U_{eq} (Cu)
U_{eq} (Se)
U_{eq} (Ba)
Cu_2
Cu_1
Ba
Se_1
Se_2
U_{iso} (M) ($Å^2$)
T (K)

Figure 9

TOC graphic